RSC Advances

ROYAL SOCIETY OF CHEMISTRY

PAPER

View Article Online
View Journal | View Issue

Check for updates

Cite this: *RSC Adv.*, 2026, **16**, 25485

Nickel-catalyzed CNTs enhancing cycle performance of Si@C anodes

Zheng Wang,[abc] Shuling Liu,*[a] Ming Li,*[bc] Bo Sun,[bc] Hao Li,[bc] Haocheng Wen,[bc] Haoqi Li,[bc] Wenyu Liu,[bc] Ruotong Liu,[bc] Dongzhu Liu,[bc] Aoxiang Kou[bc] and Xifei Li*[bc]

Received 5th March 2026
Accepted 10th April 2026

DOI: 10.1039/d6ra01911k

rsc.li/rsc-advances

The drastic volume change and interfacial instability during repeated cycles are the main obstacles hindering the practical application of silicon anodes. Micro/nano core–shell structures with nickel supports were constructed by spray drying and chemical vapor deposition (CVD) for silicon–carbon anode materials. The catalysis of nickel drives the growth of multidirectionally interconnected CNTs. This three-dimensional electron transport network effectively dissipates mechanical stress and increases the Li^+ diffusion rate. At the same time, the outer dense carbon coating can inhibit the continuous reduction of electrolyte, which is beneficial to the formation of a thin and uniform SEI. The built micro/nano core–shell structure with a three-dimensional conductive network offers the possibility to alleviate the volume expansion of silicon and stabilize the electrode/electrolyte interface. Therefore, the modified sample maintained a reversible capacity of 1265 mAh g^{-1} at 2 A g^{-1} after 400 cycles and exhibited an excellent rate capability at 6 A g^{-1} (1023 mAh g^{-1}). This unique micro/nano core–shell structure provides a feasible technical route for constructing highly stable silicon/carbon anodes.

1. Introduction

Due to its ultra-high theoretical capacity (4200 mAh g^{-1}) and suitable lithiation potential, silicon has long been regarded as the most ideal material for lithium-ion batteries.[1–3] However, the practical application of Si anodes is still severely hindered by the drastic volume changes during repeated lithiation and delithiation, which lead to structural shattering and unstable solid electrolyte interface (SEI) formation, ultimately leading to rapid capacity decay and low cycling performance.[4–8]

A widely adopted modification strategy is to construct Si/C composites that can enhance electronic conductivity and alleviate partial volume expansion.[9–12] In particular, the porous carbon framework provides a buffer against mechanical stress and helps to improve the cycling stability of the silicon–carbon anode.[13,14] Recent studies further demonstrate that carbon structures modified with transition metals can regulate charge transport pathways more effectively.[13,15–17] Transition metal modification has been widely recognized as an effective strategy to enhance the battery performance of Si/C composites. Nickel-based modification has attracted extensive attention owing to their excellent catalytic activity. Some recent studies have demonstrated that nickel can be introduced into Si/C composites in the form of nanoparticles, ionic dopants, or nickel-based alloys. As a catalyst, nickel can catalyze the growth of carbon nanotubes (CNTs), which forms a porous carbon skeleton with a continuous 3D conductivity. The proposed structure accelerates electron transport with the uniform current distribution.[15,18] Meanwhile, nitrogen coordination can additionally regulate the electronic structure of carbon materials and improve interfacial wettability. However, the porous structure is highly likely to promote the continuous decomposition of electrolytes, and relying solely on the internal network is still insufficient to fully stabilize the electrode/electrolyte interface under high current densities.[19] From the interfacial side, constructing a dense, continuous outer carbon coating is an effective strategy to suppress excessive electrolyte decomposition and stabilize the SEI.[20,21] This coating allows sufficient ion transport while restricting the direct contact between silicon materials and electrolytes, thereby improving structural integrity and cycling durability.[21–24]

Herein, this work proposes a nickel-supported micro/nano core–shell structure strategy, in which nickel catalytically grows CNTs through assisted carbon phase regulation to construct three-dimensional conductive networks. This

---

[a] *Department of Chemistry and Chemical Engineering, Shaanxi Collaborative Innovation Center of Industrial Auxiliary Chemistry & Technology, Key Laboratory of Auxiliary Chemistry and Technology for Chemical Industry, Ministry of Education, The Youth Innovation Team of Shaanxi Universities, Shaanxi University of Science and Technology, Xi'an, Shaanxi 710021, P. R. China. E-mail: shulingliu@aliyun.com*

[b] *Institute of Advanced Electrochemical Energy & School of Materials Science and Engineering, Xi'an University of Technology, Xi'an 710048, PR China. E-mail: xfli2011@hotmail.com; xfli@xaut.edu.cn; wsumolm@163.com*

[c] *Shaanxi Engineering Research Center of Key Materials for Lithium/Sodium-ion Batteries, Xi'an 710048, PR China*

structure shortens the electron/ion transport paths and dissipates the stress generated during cycling. Subsequently, a dense carbon coating was applied on the sample surface by chemical vapor deposition (CVD) to stabilize the electrode/electrolyte interface. More importantly, the carbon coating is beneficial to the formation of a thin and stable SEI film, which effectively inhibits the continuous decomposition of the electrolyte.[16,25–27] Nickel-catalyzed growth of CNTs to form a conductive network, combined with a dense and stable carbon coating deposited by CVD on the outer layer, provides a feasible way to break through the kinetic and interfacial bottleneck of Si-based anodes.[28–31]

2. Experimental

2.1 Synthesis of Si@N-C-CNTs@C

The silicon nanoparticles were dispersed in deionized water for preliminary ultrasonic dispersion. Ten mg of nickel acetate tetrahydrate was dissolved in 10 mL of deionized water to prepare a homogeneous nickel precursor solution. Subsequently, a nickel solution was added to the silicon nanoparticle suspension, followed by further sonication to ensure homogeneous mixing. Then, 500 mg of melamine ($C_3H_6N_6$), 500 mg of polyvinylpyrrolidone (PVP K82-96), and 500 mg of glucose ($C_6H_{12}O_6$) were sequentially added to the above mixture with continuous stirring until a well-dispersed solution was obtained. The resulting solution was subjected to water bath evaporation at 60 °C and concentrated to a volume of about 50 mL and then treated by spray drying to obtain Si@N-C-CNTs material powder. Then, the prepared precursor was transferred to a tube furnace and heated to 300 °C at a heating rate of 2 °C min^{-1} under an argon atmosphere, maintained isothermally for 2 h. Subsequently, the temperature was further increased to 800 °C and held for 3 h, followed by furnace cooling to room temperature naturally. The prepared Si@N-C-CNTs composite powder was placed in a CVD furnace. The furnace was heated to 900 °C at a heating rate of 10 °C min^{-1} under an argon atmosphere. After stabilization at the target temperature (900 °C), ethylene (C_2H_4) gas was introduced into the furnace for 10 minutes to initiate CVD of the carbon. Subsequently, the ethylene gas supply was terminated and naturally cooled with the furnace to room temperature under a continuous argon atmosphere to obtain the final Si@N-C-CNTs@C composite.

2.2 Materials characterization

The microstructure was observed using a scanning electron microscope (SEM, Merlin Compact). The crystal structure of the composite was investigated by means of X-ray photoelectron spectroscopy (XPS, Amicus) and X-ray diffractometer (XRD, SHIMADZU XRD-7000). Thermogravimetric analysis (TGA) curves were recorded on a TGA-500 instrument under an air atmosphere, with the temperature ramped from 30 °C to 800 °C at a heating rate of 10 °C min^{-1}. The crystallinity was determined using a Horiba LabRAM HR Evolution Raman spectrometer. The lattice fringes were analyzed, and the composition was identified by combining transmission electron microscopy (TEM, JEM-F200) with energy dispersive spectroscopy (EDS). Atomic force microscope (AFM) was used to observe the elastic modulus of the composites.

2.3 Electrochemical measurements

The active material, the conductive agent (Super P), and the binder (CMC) were mixed at a mass ratio of 8 : 1 : 1 and thoroughly ground. A certain amount of deionized water was then added, and the mixture was stirred for 9 h. Subsequently, a small amount of styrene-butadiene rubber (SBR) was incorporated and stirred for 1 hour to form a homogeneous slurry. The slurry was coated onto the copper foil using an MSK-AFA-A automatic thick film coater. The coated copper foil was dried at 60 °C for 12 h to prepare the electrode, which was then cut into discs ($\Phi = 12$ mm) and weighed for subsequent use. A lithium sheet was used as the counter electrode, and the working and counter electrodes were separated by a Celgard 2325 double layer separator ($\Phi = 16$ mm). Lithium hexafluorophosphate ($LiPF_6$) was dissolved in a mixed solvent composition of EC, EMC and DEC, and 2% vinylene carbonate and 10% fluoroethylene carbonate were added to prepare an electrolyte. All CR2032 coin half-cells were assembled in an argon-filled glove box with both H_2O and O_2 contents below 1.0 ppm. Some electrolyte (about 80 μL) was injected, and all other assembly procedures remained unchanged. Electrochemical testing of button half cells was performed on a NEWARE CT-4008. Measurements of charge–discharge performance were performed in the voltage range of 0.01–1.5 V (*vs.* Li/Li^+), and galvanostatic intermittent titration technique (GITT) tests were performed on the same platform. GITT was used to obtain Li^+ diffusion coefficients at different states of charge (SOC) and locate transport bottlenecks, calculated according to the Weppner–Huggins relation. CV was measured on a Princeton Versa STAT 4 at a scan rate of 0.1/0.3/0.5/0.7/0.9/1.0 mV s^{-1} at 0.01–1.5 V (*vs.* Li/Li^+). Electrochemical impedance spectroscopy (EIS) was analyzed at frequencies of 100 kHz–0.01 Hz, EIS spectra at different voltages were detected by DRT technique, and *in situ* EIS was collected along 0.01–1.5 V charge/discharge trajectories.

2.4 Finite element simulation

The finite element simulation was completed using COMSOL Multiphysics 6.3 software equipped with MEMS module, battery module and CAD import module. In this study, two three-dimensional models were constructed to characterize the composite electrode structure. Si@N-C-CNTs is a silicon nanoparticle structure modified by transition metal catalyzed growth of CNTs on a carbon coated substrate. Si@N-C-CNTs@C is obtained by depositing a dense carbon coating on the basis of Si@N-C-CNTs structure. This simulation aims to evaluate the mechanical stress caused by the volume expansion of silicon during lithiation, and the distribution of stress in the carbon coating, CNTs and outer dense carbon coating.

3. Results and discussion

Fig. 1 shows the schematic illustration for the fabrication of the 3D conductive networked micro/nano core–shell structure. Initially, with silicon nanoparticles as the core, nickel

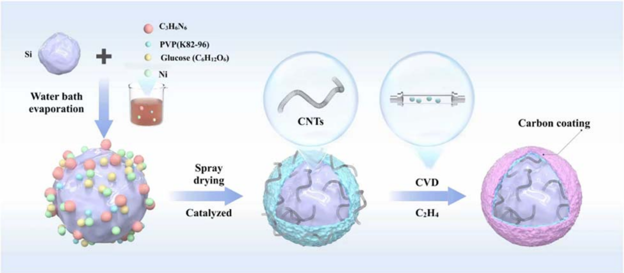

Fig. 1 The synthesis schematic of the Si@N-C-CNTs@C composites.

precursors and nitrogen-containing organic ligands ($C_3H_6N_6$) were introduced into the system, and nickel-loaded micro/nano structured silicon carbon materials were prepared *via* spray drying. During treatment at 800 °C, Ni^{2+} anchored on the silicon surface through Ni–N_X coordination is subsequently reduced to nickel nanoparticles, which serve as the active sites for the catalytic growth of CNTs. The carbon source originates from the pyrolysis of glucose, PVP, and melamine, which are decomposed into carbon atoms on the surface of nickel nanoparticles. The carbon atoms continuously deposit and directionally grow along the crystal planes of nickel nanoparticles, finally forming a multidimensionally interconnected CNTs network on the silicon surface to accelerate ion transport.[15,32] On this basis, ethylene (C_2H_4) was introduced as an exogenous carbon source for CVD treatment. It is speculated that the residual nickel nanoparticles on the surface of pre-formed CNTs may further play a catalytic role to promote the decomposition of C_2H_4 into carbon atoms. These carbon atoms are then grown on the original CNTs skeleton to form CNTs segments.[33] Under the continuous catalysis of nickel, the denser and more penetrating 3D CNTs networks may be deposited onto the silicon surface. The nickel-catalyzed CNTs synergistically act with the outer dense carbon coating, which can inhibit the electrolyte decomposition and facilitate the formation of thin and stable SEI.

The morphological characteristics of the three composites are shown in Fig. 2a–c, S1 and S2. It can be observed that the composites prepared *via* spray drying exhibit a spherical morphology. The local filamentous structures can be clearly observed in the high-magnification images, which are the typical characteristics of CNTs. It is preliminarily inferred that the introduction of nickel can catalyze the growth of CNTs, forming an interconnected conductive network and providing buffer space to alleviate the volume expansion.[34,35] In comparison to Si@N-C-CNTs Si@N-C-CNTs@C exhibited obvious dense CNTs network, as shown in Fig. 2c and S2. It may be related to the further growth of CNTs caused by nickel catalyzing ethylene at high temperatures. In addition, the thickness of the carbon coating is also a key factor affecting the morphology of the outer coating, revealing that the outer carbon coating may lead to the exposure of CNTs.[36]

The X-ray diffraction (XRD) pattern in Fig. 2d reveals that the characteristic diffraction peaks of crystalline silicon in the three composite samples appear at 28.4°, 47.3°, and 56.1°, corresponding to the (111), (220), and (311) crystal planes of crystalline silicon, respectively. This indicates that the crystal structure of silicon remains intact throughout the ultrasonic hydrothermal treatment, spray drying, and high-temperature carbonization. Furthermore, in the X-ray diffraction patterns, Si@N-C-CNTs and Si@N-C-CNTs@C showed unique shoulder peaks associated with nickel-containing crystalline phases compared to Si@N-C, which confirmed that nickel has been successfully doped into this material.

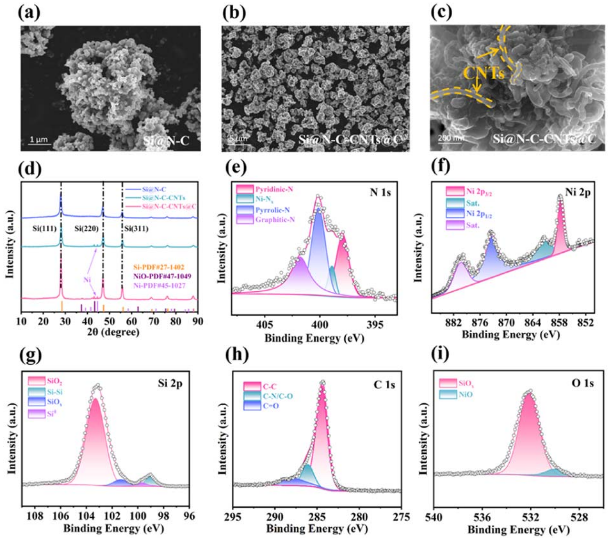

Fig. 2 (a) SEM images of Si@N-C. (b and c) SEM images of Si@N-C-CNTs@C. (d) The XRD patterns of Si@N-C, Si@N-C-CNTs and Si@N-C-CNTs@C. (e–i) XPS patterns of Si@N-C-CNTs@C. The fitted high-resolution maps of (e) N 1s, (f) Ni 2p, (g) Si 2p, (h) C 1s and (i) O 1s.

X-ray photoelectron spectroscopy (XPS) measurements were performed to analyze the surface composition of Si@N-C-CNTs@C (Fig. 2e–i and S3). In the high-resolution N 1s XPS spectra, the binding energies of pyridine-*N*, pyrrole-*N*, and graphite-*N* were 398.2 eV, 400.1 eV, and 402.2 eV, respectively. Pyridine-*N* and pyrrole-*N* can provide abundant lithiophilic active sites, which significantly enhances the contribution of pseudocapacitance. The Si@N-C-CNTs@C exhibited a stronger graphite-*N* signal after carbon deposition, which helped to enhance the conductivity of the carbon matrix.[37] Meanwhile, the Ni–N_X coordination at 399.1 eV confirms that nickel is anchored by nitrogen sites for stable dispersion, which also endows the anode with abundant lithiophilic active sites and thus enhances the electrode's Li^+ adsorption capacity. The high-resolution Ni 2p XPS spectrum (Fig. 2f) shows that the Ni $2p_{3/2}$ Ni $2p_{1/2}$ and satellite peaks are located at 855.2, 873.2 eV and 861.6, 881.4 eV, confirming that nickel is in the Ni^{2+} valence state. Nickel is reduced to highly dispersed nickel nanoparticles at elevated temperatures. As a catalytic core, these nanoparticles induce the cleavage of carbon sources and the *in situ* growth of CNTs. Meanwhile, it is possible to maintain continuous catalytic activity during the subsequent CVD process to catalyze ethylene decomposition and drive further extension of CNTs to form interconnected 3D conductive networks.[38] The high-resolution

Si 2p XPS spectra (Fig. 2g) showed the presence of Si–O bonds (103.5 eV), indicating that slight oxidation occurred on the Si surface. This forms a SiO_x transition layer between the Si core and the carbon coating to suppress side reactions. High-resolution C 1s XPS spectra (Fig. 2h) showed characteristic peaks at 284.65 eV, 285.6 eV, and 289 eV, corresponding to C–C, C–N, and C=O bonds, confirming the formation of an external dense carbon shell with an N-doped internal carbon framework. This polar functional group provides an active site for SEI nucleation and endows the material with lithiophilicity. The C=O bonds are mainly derived from surface oxidation of carbon materials and precursor residues. Furthermore, the high-resolution O 1s XPS spectroscopy (Fig. 2i) showed that the oxygen signal was dominated by Si–O bonds with only trace amounts of NiO. This indicates that nickel mainly exists in the Ni–N_X coordination state and has a low oxidation degree during the material preparation process.

As evidenced by the elemental mapping images in Fig. 3a and S4–S7, the presence and successful doping of Ni are further confirmed. Nickel is uniformly dispersed on both carbon coating and CNTs, in the form of discrete nano-sites without obvious agglomeration. This highly dispersed structure is more likely to leave the nickel nanoparticles, maintain the catalytic activity in the subsequent CVD process, and promote the further growth and extension of the CNTs.

High-resolution transmission electron microscopy (HRTEM) images (Fig. 3b and c) show that the layer spacing of region (I) is 0.336 nm, corresponding to the planar spacing of the Si (111) crystal plane, which has an average planar spacing of 0.3 nm.[39] The carbon coating with a thickness of 10.33 nm was measured on the material surface, which verified that the Si@N-C-CNTs material successfully deposited a dense amorphous carbon coating by CVD deposition process. Furthermore, SAED patterns acquired from the same region are presented separately to distinguish different crystalline phases. As shown in Fig. 3d, diffraction rings attributable to the Ni (110) and Ni (210) crystal planes can be clearly observed, confirming the presence of crystalline metallic nickel in the composite material.[40] Diffraction rings corresponding to Si (111), Si (220), and Si (311) crystal planes are observed in Fig. S10, and the diffraction characteristics of Ni and Si coexist in the same region. This further confirms that Ni was successfully introduced and formed intimate contact with silicon particles. Direct structural evidence is provided for the Ni-catalyzed generation of CNTs to construct internal conductive carbon networks.

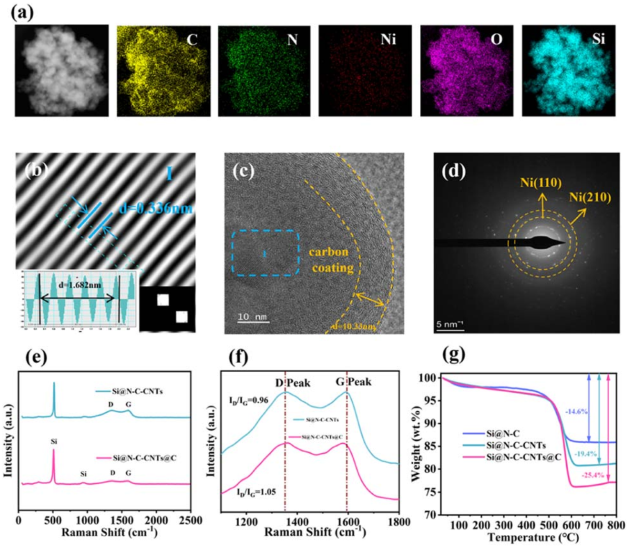

Fig. 3 (a) Elemental mapping of Si@N-C-CNTs@C. (b–d) TEM and HRTEM of Si@N-C-CNTs@C. (e and f) Raman spectra, (g) TG analysis.

Raman spectroscopy (Fig. 3e and f) was used to further investigate the crystallinity of carbon. The D-band and G-band of carbon are represented by two characteristic peaks at 1348 cm^{-1} and 1580 cm^{-1}, respectively. The relatively high I_D/I_G intensity ratio indicates a high degree of amorphous carbonization.[41] The I_D/I_G value is 0.96 for Si@N-C-CNTs and 1.05 for Si@N-C-CNTs@C, suggesting that the introduction of CNTs and the carbon coating introduced appropriate amounts of disordered carbon and polar functional group sites, which could provide Li^+ adsorption sites and promote pseudocapacitive effect generation.

Thermogravimetric analysis (TGA) was performed on Si@N-C, Si@N-C-CNTs, and Si@N-C-CNTs@C composites, with the curves shown in Fig. 3g. Si@N-C-CNTs and Si@N-C-CNTs@C exhibited a continuous and slow weight loss in the temperature range of 100–400 °C. This reflects that nickel exerts a certain catalytic effect on carbon oxidation and advances the initiation temperature of carbon oxidation.[42] Significant weight loss occurred for all three samples at approximately 420–560 °C, compared to Si@N-C-CNTs@C showing a significantly higher weight loss, indicating that it contains a higher content of combustible carbon due to its dense outer carbon coating. Above 560 °C, the three curves tend to stabilize at the plateau, showing excellent thermal stability. Overall, the TGA results validate the effectiveness of the carbon coating strategy. The conductive carbon coating of Si@N-C-CNTs@C facilitates the construction of an electrochemical conductive network and alleviate expansion stress.

The electrochemical performance of Si@N-C-CNTs@C was tested in a half-cell system. The cyclic voltammetry (CV) profiles are presented in Fig. 4a and S11. CV measurements were conducted on both Si@N-C-CNTs and Si@N-C-CNTs@C electrodes at a scan rate of 0.1 mV s^{-1} within the voltage window of 0.01–1.5 V, aiming to analyze their electrochemical reaction processes and thus investigate interfacial stability and reversibility. As observed from the profiles, the two materials exhibit similar CV curves, with a distinct reduction peak at 0.23 V, which corresponds to the formation of the amorphous silicon alloy phase and the lithium intercalation process. During the subsequent charging process, two oxidation peaks emerge at approximately 0.36 V and 0.53 V; these peaks are associated with the dealloying process of silicon, representing the further dealloying transition from the highly lithiated phase to the low-lithiated phase. A broad peak at 0.8 V is attributed to the reduction of the electrolyte and the formation of the solid electrolyte interphase (SEI) film. The oxidation and reduction peaks of the two materials almost overlap, indicating the

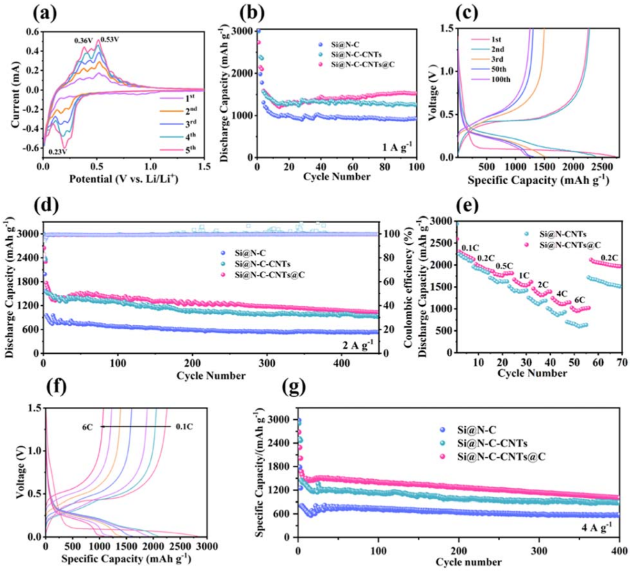

Fig. 4 (a) CV curves and (b) Cycling performance of Si@N-C-CNTs@C, Si@N-C-CNTs, and Si@N-C at 1 A g^{-1}. (c) (Dis)charging curves of Si@N-C-CNTs@C. (d) Cycling stability and coulombic efficiency of Si@N-C-CNTs@C, Si@N-C-CNTs, and Si@N-C at 2 A g^{-1}. (e) Rate capability. (f) The charge–discharge at different current density of Si@N-C-CNTs@C. (g) Cycling performance of Si@N-C-CNTs@C, Si@N-C-CNTs, and Si@N-C at 4 A g^{-1}.

absence of obvious side reactions during lithium-ion insertion/extraction processes.[43] Notably, the peaks of Si@N-C-CNTs@C is sharper with higher peak currents, suggesting lower charge transfer resistance and smaller polarization. With increasing scan cycles, the peak intensities of both oxidation and reduction peaks gradually increase, which is indicative of the continuous activation of the silicon material.

The charge–discharge curves of the Si@N-C-CNTs@C composite were measured at a current density of 1 A g^{-1} within the operating voltage range of 0.01–1.5 V. It can be observed that a long voltage plateau below approximately 0.1 V exists in the initial discharge curve of both materials, which arises from the alloying reaction of crystalline silicon during lithium intercalation, leading to the formation of the amorphous Li_XSi phase. To further investigate the effect of introducing dense carbon coating and CNTs on the electrochemical properties of the composites, cyclic performance tests of Si@N-C, Si@N-C-CNTs, and Si@N-C-CNTs@C were performed (as shown in Fig. 4b). The initial discharge capacity of Si@N-C-CNTs@C is 2561 mAh g^{-1} and that of Si@N-C-CNTs is 2905 mAh g^{-1}, while the initial discharge capacity of Si@N-C is 3011 mAh g^{-1}, which maintains a specific discharge capacity of 1540 mAh g^{-1} after 100 cycles at a current density of 1 A g^{-1}, higher than that of Si@N-C-CNTs (1250 mAh g^{-1}) and Si@N-C (920 mAh g^{-1}). As shown in Fig. S12a, the charge/discharge specific capacities of Si@N-C-CNTs at the 1st, 3rd, and 100th cycles are 1700/2906 mAh g^{-1}, 1508/1951 mAh g^{-1}, and 717/822 mAh g^{-1}, respectively. The charge curves shift progressively toward higher voltages, reflecting the rapid accumulation of polarization and interfacial resistance. Severe volume expansion occurs during cycling, resulting in rapid capacity decay and poor cycling reversibility. In contrast, as shown in Fig. S12b, the charge/discharge specific capacities of Si@N-C-CNTs@C at the 1st, 3rd, and 100th cycles are 1909/2589 mAh g^{-1}, 1760/1857 mAh g^{-1}, and 1136/1240 mAh g^{-1}, respectively. Compared with Si@N-C-CNTs, Si@N-C-CNTs@C displays higher curve overlap and smaller hysteresis at the same cycle numbers, demonstrating superior charge transfer and ion diffusion kinetics, as well as a higher reversible capacity. These results indicate that the outer dense carbon coating effectively suppresses side reactions and electrolyte penetration, facilitates the formation of a stable and thin SEI film, and consequently contributes to a higher initial coulombic efficiency (ICE) and better capacity retention.[44]

Fig. 4e shows the rate performance of Si@N-C-CNTs, Si@N-C-CNTs@C at current densities ranging from 0.1–6C. Si@N-C-CNTs@C provides discharge capacities of 2337, 2075, 1763, 1644, 1523, 1284, and 1023 mAh g^{-1} at various rates, all outperforming Si@N-C-CNTs. When the current density recovered to 0.2 A g^{-1}, the capacity of Si@N-C-CNTs@C quickly recovered to the initial level, demonstrating the excellent rate capability of the composite. Meanwhile, the cycling performance of the three materials at 2 A g^{-1} and 4 A g^{-1} current densities was also investigated (Fig. 4d and g). Si@N-C-CNTs@C exhibits much better cycling stability, maintaining a reversible specific capacity of 1265 mAh g^{-1} after 400 cycles with a capacity retention rate of 80%, which is higher than that of Si@N-C and Si@N-C-CNTs. Even at a high current density of 4 A g^{-1}, Si@N-C-CNTs@C still exhibits higher reversible specific capacity than the other two samples and has good cycling stability. These results confirm that Ni-catalyzed CNTs networks construct 3D continuous electron transport paths between particles and provide void spaces to buffer volume changes.[21,45] More importantly, under the continuous catalytic action of nickel, the dense outer carbon coating deposited *via* CVD minimizes the surface exposure of silicon, inhibits the deep penetration of electrolyte, and promotes the formation of a uniform SEI, thereby effectively alleviating the severe volume expansion of silicon during cycling.[21]

Both the three-dimensional CNTs and the dense carbon coating provide synergistic mechanism of performance improvement. The three-dimensional CNTs network catalyzed by nickel resolves the intrinsic structural drawbacks of silicon-based anodes, including poor electrical conductivity and drastic volume expansion. Meanwhile, the dense carbon coating addresses the interfacial issues of instability and repeated SEI fracture and regeneration. The synergistic improvement of electrochemical performance is achieved through the dual optimization of structure and interface.

To investigate the electrochemical reaction kinetics of Si@N-C-CNTs and Si@N-C-CNTs@C electrode materials, cyclic voltammetry (CV) measurements were performed at varying scan rates from 0.1 to 1.0 mV s^{-1} (as shown in Fig. 5a and b). Both sets of samples exhibit similar CV profiles. With increasing scan rate, the peak currents of all samples gradually rise, and the Si@N-C-CNTs@C electrode delivers the highest peak current. As the scan rate continues to increase, the peak currents of all

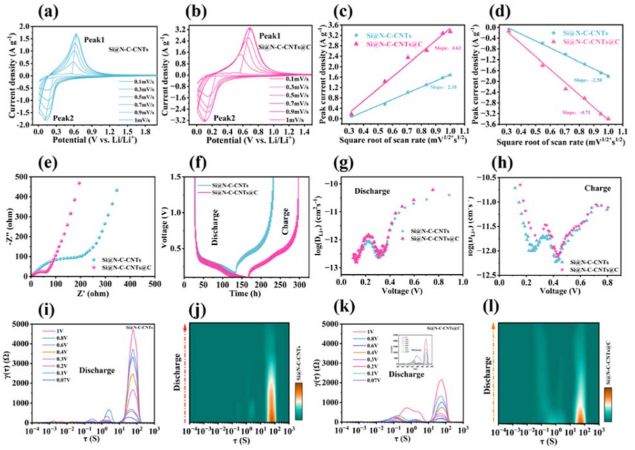

Fig. 5 (a and b) CV curves at scanning rates from 0.1 to 1.0 mV s^{-1} of Si@N-C-CNTs@C and Si@N-C-CNTs. (c and d) The relationship between scan rate squared and peak current density. (e) Nyquist plots of Si@N-C-CNTs and Si@N-C-CNTs@C. (f) GITT curves of Si@N-C-CNTs and Si@N-C-CNTs@C. $D_{\mathrm{Li^+}}$ of Si@N-C-CNTs and Si@N-C-CNTs@C during (g) discharging and (h) charging. The DRT transformation of *in situ* EIS spectra for (j) Si@N-C-CNTs and (l) Si@N-C-CNTs@C during the discharge. (i and k) DRT curves of *in situ* EIS spectra of Si@N-C-CNTs and Si@N-C-CNTs@C during the discharge.

samples show an upward trend accompanied by slight peak shifts. The Si@N-C-CNTs@C exhibits the maximum and minimum slopes at peak 1 and peak 2, respectively (Fig. 5c and d), indicating that it possesses the fastest $\mathrm{Li^+}$ diffusion kinetics. Electrochemical impedance spectroscopy (EIS) measurements (Fig. 5e) demonstrate that the charge transfer resistance (R_{ct}) of Si@N-C-CNTs@C is lower than that of Si@N-C-CNTs, confirming that the presence of the dense carbon coating effectively reduces the R_{ct}.[46] Galvanostatic intermittent titration technique (GITT) measurements were carried out on Si@N-C-CNTs and Si@N-C-CNTs@C electrodes, and Fig. 5f shows the voltage-time curves of the electrode materials, which are essential for accurately evaluating $\mathrm{Li^+}$ diffusion within the electrodes. Based on the GITT results, the $\mathrm{Li^+}$ diffusion coefficient ($D_{\mathrm{Li^+}}$) was calculated using the following equation:

$$D_{\mathrm{Li^+}} = \frac{4L^2}{\pi\tau}\left(\frac{\Delta E_{\mathrm{s}}}{\Delta E_{\mathrm{t}}}\right)^2 \tag{1}$$

The $D_{\mathrm{Li^+}}$ value increases correspondingly with the increase in ΔE_{s} and the decrease in ΔE_{t}.[47] As shown in Fig. 5f and g, the locally magnified GITT curves of Si@N-C-CNTs and Si@N-C-CNTs@C are presented in Fig. S17 and S18, respectively. The results in Fig. 5g and h reveal that the $\mathrm{Li^+}$ diffusion coefficient of Si@N-C-CNTs@C is higher than that of Si@N-C-CNTs during the charge–discharge processes. This verifies that the dense carbon coating restricts the deep penetration of electrolyte, facilitating the formation of a thinner and more uniform LiF-rich SEI film. In addition, the Ni-catalyzed CNTs construct a 3D conductive network, which provides continuous electron transport pathways and buffers mechanical stress, thus effectively enhancing the electrical conductivity of the composite. Nitrogen doping improves the carrier density and surface polarity of the carbon phase, which is conducive to increasing the $\mathrm{Li^+}$ diffusion coefficient of the composite. *In situ* EIS measurements were conducted to evaluate the dynamic parameters of the electrodes during the discharge process of cycling (Fig. 5i–k). The impedance spectra of Si@N-C-CNTs and Si@N-C-CNTs@C at different voltages, presented in Fig. S19, were used as the original data for distribution of relaxation times (DRT) transformation, while Fig. S21 shows the DRT transformation results of the electrode during the charge process of cycling. Compared with Si@N-C-CNTs, Si@N-C-CNTs@C exhibits significantly lower charge transfer resistance and diffusion impedance during electrochemical cycling. This confirms that the dense carbon coating effectively suppresses the regeneration and thickening of SEI and constructs a continuous, highly conductive outer surface. This effect is directly confirmed by the smaller semicircle in the *in situ* EIS profile and its smoother evolution with applied potential. DRT is a technique that avoids fitting errors by directly determining the time constants of electrochemical processes from EIS data.[47] Therefore, the DRT function reflects dynamic information. As shown in the DRT curves, peak (i) at relaxation times >10 s (R_{D}) is attributed to the solid-phase $\mathrm{Li^+}$ diffusion, as well as the concentration polarization diffusion in porous electrodes and electrolyte phase. Peak (ii) in the range of 10^{-2}–10 s (R_{ct}) corresponds to the charge transfer resistance at the material surface. Peak (iii) at relaxation times $<10^{-2}$ s (R_{SEI}) represents the interfacial reaction at the SEI film. Compared with Si@N-C-CNTs, Si@N-C-CNTs@C has lower R_{D} and R_{ct} values, indicating faster and more uniform $\mathrm{Li^+}$ transport in its solid phase and porous structure. This is the fundamental reason for its lower polarization, superior rate capability, and more stable cycling performance. At a voltage of approximately 0.8 V, the R_{ct} and R_{D} peaks of Si@N-C-CNTs@C increase sharply, which is due to the formation of the SEI film. Therefore, the introduction of the dense carbon coating layer limits electrolyte penetration, enabling the formation of a thin and uniform SEI film in the first cycle, which effectively improves structural stability. The 3D electron transport pathway constructed by the carbon layer and CNTs reduces contact impedance, thus significantly enhancing the structural stability and $\mathrm{Li^+}$ diffusion rate of the material.[48–51]

As shown in Fig. 6a and c, the Si@N-C-CNTs@C electrode had an initial thickness of about 12.3 μm before cycling, which increased to 14.1 μm after cycling. There is approximately 17% thickness expansion. In contrast, the thickness of the Si@N-C-CNTs electrode (Fig. 6b and d) significantly increased from 22.5 μm to 28.35 μm, indicating that it experienced a drastic volume expansion of about 28% during repeated lithiation/delithiation. Notably, the cycled Si@N-C-CNTs@C electrode maintains a relatively dense and continuous cross-sectional morphology without obvious cracking or delamination. While the Si@N-C-CNTs electrode shows significant structural damage and electrode expansion. The substantially suppressed thickness expansion of the Si@N-C-CNTs@C electrode demonstrates that the carbon coating effectively accommodates

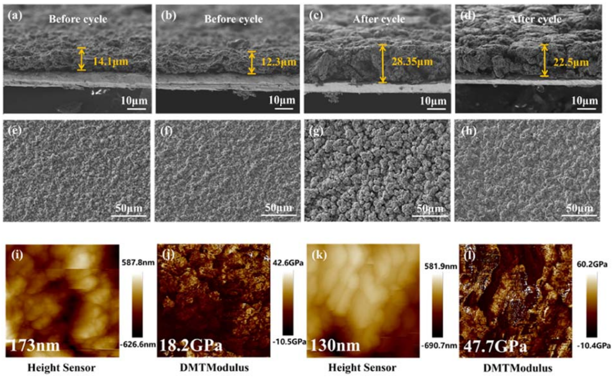

Fig. 6 Cross-sectional morphology of electrodes before and after cycling. (a and c) Si@N-C-CNTs@C composite electrode; (b and d) Si@N-C-CNTs composite electrode. Top-view morphology before 100 cycles of (e) Si@N-C-CNTs and (f) Si@N-C-CNTs@C. Top-view morphology after 100 cycles of (g) Si@N-C-CNTs and (h) Si@N-C-CNTs@C. The surface roughness after cycle (i) Si@N-C-CNTs electrode, and (k) Si@N-C-CNTs@C electrode. The young's modulus mapping of cycled (j) Si@N-C-CNTs electrode and (l) Si@N-C-CNTs@C electrode.

the volume change of silicon and preserves electrode integrity during long-term cycling.[49–51]

Fig. 6e–h displays the surface morphology changes of Si@N-C-CNTs@C and Si@N-C-CNTs electrodes before and after cycling. Before cycling (Fig. 6e and f), both electrodes exhibited a relatively uniform and dense surface structure with continuous particle distribution, and no obvious cracks or peeling phenomena were observed. This indicates that the as-prepared electrodes possess excellent structural integrity and interfacial uniformity. After long-term cycling, the surface morphologies of the two electrodes showed distinct differences. As shown in Fig. 6g, the surface of the Si@N-C-CNTs electrode underwent significant roughening and particle agglomeration, accompanied by the formation of microcracks. These features reflect the continuous structural damage to the electrode surface caused by the volume expansion of silicon during repeated lithiation/delithiation processes. In contrast, the cycled Si@N-C-CNTs@C electrode (Fig. 6h) maintained a relatively intact and continuous surface morphology, with only slight surface undulations observed and no obvious cracks or large-scale structural collapse detected. This demonstrates that its surface structure has superior stability during the cycling process. The combined changes in surface and cross-sectional morphologies indicate that the dense outer carbon coating of Si@N-C-CNTs@C electrode further suppresses the volume expansion of Si during cycling and stabilizes the electrode and electrolyte interface.[52,53]

Atomic Force Microscopy (AFM) was employed to characterize the surface morphology and mechanical properties of the electrodes after cycling. As shown in Fig. 6i and k, the surface height undulation of the Si@N-C-CNTs electrode is about 168 nm, while the surface height undulation of the Si@N-C-CNTs@C electrode drops to about 139 nm. This indicates that the dense outer carbon coating is beneficial to maintain the structural integrity of the electrode. The corresponding DMT modulus mappings (Fig. 6j and l) further reveal a remarkable difference in mechanical stiffness between the two electrodes. The average DMT modulus of Si@N-C-CNTs is around 18.2 GPa, whereas that of Si@N-C-CNTs@C increases significantly to 47.7 GPa. This significant enhancement of the effective surface modulus indicates that the dense carbon coating homogenizes the stress distribution and suppresses the local expansion stress during cycling. Consequently, improving the structural stability contributes to the stabilization of the electrode/electrolyte interface and supports the excellent cycling performance of the Si@N-C-CNTs@C electrode.

As shown in Fig. 7a and d, the LiF characteristic signal (685 eV) of the Si@N-C-CNTs@C anode is more significant compared to the Si@N-C-CNTs anode. This phenomenon shows that the dense carbon coating promotes the enrichment of the inorganic SEI component (LiF) with high mechanical strength and superior ionic conductivity. The LiF-rich SEI film exhibits excellent structural stability, effectively reduces the interfacial charge-transfer resistance and improves Li^+ transport efficiency. After 10 cycles, the high-resolution Li 1s XPS spectra of the electrodes is shown in Fig. S23. Compared with the Si@N-C-CNTs anode, the Si@N-C-CNTs@C anode exhibits a significantly higher intensity of the Li 1s characteristic peak, indicating that the dense carbon coating effectively promotes the enrichment of stable Li-containing components (LiF) in the SEI film, and suppresses the irreversible consumption of Li^+. In the C 1s photoelectron spectrum Fig. 7b and e, both Si@N-C-CNTs and Si@N-C-CNTs@C anodes showed C–C, C–O, and R_2CO_2Li (290 eV) characteristic peaks. These peaks are derived from the decomposition products of organic components in the electrolyte, such as dimethyl carbonate (DMC), ethylene carbonate (EC) and ethyl carbonate (EMC). It is worth noting that the R_2CO_2Li signal of the Si@N-C-CNTs@C anode at 290 eV is significantly weakened, indicating that the polar functional groups (C–C, C–O) on the surface of the dense carbon coating provide uniform nucleation sites for SEI formation, which contributes to the rapid generation of a thin and uniform SEI

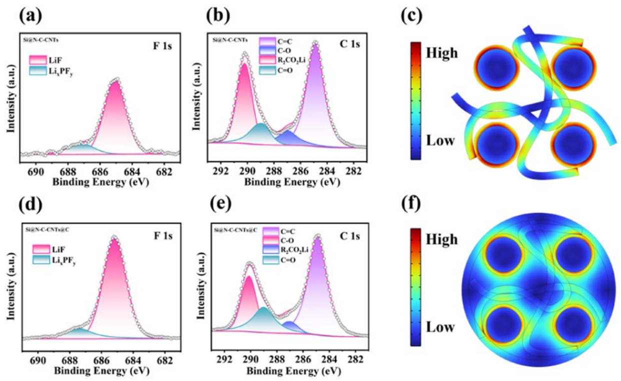

Fig. 7 The (a) F 1s and (b) C 1s spectra of Si@N-C-CNTs electrode after 10 cycles. The (d) F 1s and (e) C 1s spectra of Si@N-C-CNTs@C electrode after 10 cycles. (c and f) The stress distribution of Si@N-C-CNTs and Si@N-C-CNTs@C.

film during the initial discharge. Meanwhile, the decomposition of organic electrolytes is significantly suppressed at the electrode/electrolyte interface, thus reducing the formation of organic SEI components (R_2CO_2Li). The dense and continuous carbon coating forms a physical barrier, which prevents the direct contact between active silicon and the electrolyte as well as the continuous reduction of electrolyte, thus avoiding excessive consumption of lithium and electrolyte. Meanwhile, benefiting from its excellent flexibility, it can buffer the volume expansion of silicon during lithiation/delithiation, maintain the integrity of the electrode/electrolyte interface, and prevent electrode cracking.

The mechanical behaviors of Si@N-C-CNTs and Si@N-C-CNTs@C were compared by finite element simulations. The initial model and detailed data are shown in Fig. S24, S25 and Table S1. The Young's modulus, Poisson's ratio, and yield stress of Si@N-C-CNTs@C are listed in Table S2. The finite element simulation uses the typical mechanical parameters of each component in the table to calculate the mechanical response and stress distribution of the composite electrode during lithiation.

As shown in Fig. 7c and f, Si@N-C-CNTs show obvious stress concentration at the interface between silicon particles and CNTs, indicating that the carbon tube network has limited buffering capacity for the severe volume expansion of silicon during lithiation, and long-term cycling is easy to cause the pulverization of active materials and the collapse of electrode structure. In contrast, the overall stress level of Si@N-C-CNTs@C is significantly reduced, and the high stress region is effectively confined near the boundary between the silicon particles and the outer carbon coating. On the basis of CNTs, the external dense carbon coating further enhances the stress buffering effect of the silicon anode, providing important support for improving the structural integrity and cycle stability of the electrode.

In summary, the dense carbon coating could suppress the decomposition of organic electrolyte, significantly reduce the electrode/electrolyte interfacial resistance and improve Li^+ transport efficiency, homogenizing the stress distribution during cycling. It confines the high-stress region to the interface between silicon particles and the carbon coating, and alleviates the severe volume expansion of silicon anodes. The dual optimization of mechanical strength and ion transport by the dense carbon coating is the key reason for the significantly improved cycling performance and rate capability of the Si@N-C-CNTs@C composite.

4. Conclusions

In conclusion, the prepared Si@N-C-CNTs@C composite exhibits excellent cycling stability and rate capability. The improved electrochemical performance is due to the synergistic effect between nickel catalysis and the dense carbon coating. The catalytic effect of nickel nanoparticles induces the formation of interconnected CNTs, which facilitates continuous electron transport and relieves the volume expansion stress during cycling. With ethylene as the carbon source for subsequent CVD modification, the nickel nanoparticles maintain sustained catalytic activity and further catalyze ethylene decomposition, driving the directional extension and interconnection of the original CNTs to form a denser three-dimensional conductive network. Moreover, the dense carbon coating deposited by CVD stabilizes the electrode/electrolyte interface and inhibits electrolyte decomposition, favoring the formation of a thin and uniform SEI. The synergistic effect of the three-dimensional CNTs and the dense carbon coating alleviate the volume expansion of silicon and stabilize the electrode/electrolyte interface. It exhibits excellent rate capability and long-term cycle stability with the specific capacity of 1265 mAh g^{-1} after 400 cycles at 2 A g^{-1}. This work shows that the synergistic effect of the internal carbon structure catalyzed by transition metal and the dense outer carbon coating provides practical theoretical and practical guidance for the design of silicon-based anode.

Author contributions

This study was designed, supervised, and critically revised with the generous support and dedicated efforts of professor Xifei Li, professor Shuling Liu, and Dr Ming Li. Zheng Wang conceived and performed the experiments, synthesized and characterized the materials, and drafted the initial manuscript. Dr Bo Sun and Hao Li analyzed the experimental results and contributed to manuscript preparation. Haoqi Li, Haocheng Wen, Wenyu Liu, Ruotong Liu, Dongzhu Liu, and Aoxiang Kou participated in the material testing.

Conflicts of interest

There are no conflicts to declare.

Data availability

All data supporting the findings of this study are available within the article and its supplementary information (SI). Additional raw data are available from the corresponding author upon reasonable request. Supplementary information is available. See DOI: https://doi.org/10.1039/d6ra01911k.

Acknowledgements

The work was supported by the National Natural Science Foundation of China (22278255 and W2441017), Shaanxi Provincial Key Research and Development Program Project (2025CY-YBXM-025), the S&T Program of Energy Shaanxi Laboratory (ESLB202402), Sanqin Talent Special Support Program for Innovation and Entrepreneurship Teams, and the Graduate Innovation Fund of Shaanxi University of Science and Technology, China.

Notes and references

1 M. N. Obrovac and V. L. Chevrier, *Chem. Rev.*, 2014, **114**, 11444–11502.

2 A. Magasinski, P. Dixon, B. Hertzberg, A. Kvit, J. Ayala and G. Yushin, *Nat. Mater.*, 2010, **9**, 353–358.

3 X. Han, L. Gu, Z. Sun, M. Chen, Y. Zhang, L. Luo, M. Xu, S. Chen, H. Liu, J. Wan, Y.-B. He, J. Chen and Q. Zhang, *Energy Environ. Sci.*, 2023, **16**, 5395–5408.

4 L. Sun, Y. Liu, R. Shao, J. Wu, R. Jiang and Z. Jin, *Energy Storage Mater.*, 2022, **46**, 482–502.

5 E. Peled and S. Menkin, *J. Electrochem. Soc.*, 2017, **164**, A1703.

6 Y. Li, Q. Li, J. Chai, Y. Wang, J. Du, Z. Chen, Y. Rui, L. Jiang and B. Tang, *ACS Mater. Lett.*, 2023, **5**, 2948–2970.

7 Z. He, L. Liu, S. Liu, Y. Chen, L. Sun, C. Liu, Y. Zhu and X. Wang, *Chem. Eng. J.*, 2023, **472**, 144991.

8 H. Zhao, J. Li, Q. Zhao, X. Huang, S. Jia, J. Ma and Y. Ren, *Electrochem. Energy Rev.*, 2024, **7**, 11.

9 H. Wang, J. Fu, C. Wang, J. Wang, A. Yang, C. Li, Q. Sun, Y. Cui and H. Li, *Energy Environ. Sci.*, 2020, **13**, 848–858.

10 J.-y. Ock, M. Lehmann, C. Li, Y. Wang, H. M. Meyer Iii, A. P. Sokolov, Z. Fu and X. C. Chen, *J. Mater. Chem. A*, 2025, **13**, 24511–24521.

11 M. Han, Y. Mu, L. Wei, L. Zeng and T. Zhao, *Carbon Energy*, 2024, **6**, e377.

12 Y. Cao, T. D. Hatchard, R. A. Dunlap and M. N. Obrovac, *J. Mater. Chem. A*, 2019, **7**, 8335–8343.

13 P. Yu, Z. Li, D. Zhang, Q. Xiong, J. Yu and C. Zhi, *Adv. Funct. Mater.*, 2025, **35**, 2413081.

14 B. Jin, L. Liao, X. Shen, Z. Mei, Q. Du, L. Liang, B. Lei and J. Du, *Metals*, 2025, **15**, 386.

15 H. Zhou, H. P. Zhou, B. Yang, C. Liu, S. Zhang, T. T. Feng, Z. Q. Xu, Z. X. Fang and M. Q. Wu, *Appl. Surf. Sci.*, 2023, **640**, 158355.

16 T. Nguyen, C.-K. Yang and Y.-S. Su, *J. Alloys Compd.*, 2025, **1022**, 179886.

17 H. E. Kang, J. Ko, S. G. Song and Y. S. Yoon, *Carbon*, 2024, **219**, 118800.

18 Y. Zhao, X. Pan, M. Liu, X. Chen, R. Zhang and X. Zhiyong, *RSC Adv.*, 2023, **13**, 35026–35039.

19 F. Dong, M. Wu, Z. Chen, X. Liu, G. Zhang, J. Qiao and S. Sun, *Nano-Micro Lett.*, 2021, **14**, 36.

20 N. M. Saidi, M. A. A. M. Abdah, M. N. Mustafa, R. Walvekar, M. Khalid and A. Khosla, *Battery Energy*, 2025, **4**, e20240048.

21 Y.-S. Hsiao, H.-S. Tseng, L.-Y. Weng, S.-W. Liao, J.-H. Huang, W. K. Pang, S.-C. Hsu, H. C. Weng and Y.-C. Huang, *J. Taiwan Inst. Chem. Eng.*, 2025, **173**, 106148.

22 X. Wang, Y. Li, X. Wang, Q. Gan, Z. Wang, K. Liao, S. Wu, H. Guo, J. Li, B. Huang and Z. Lu, *J. Mater. Chem. A*, 2023, **11**, 9807–9815.

23 A. D. Refino, N. Yulianto, S. Priyono, M. Manawan, R. F. H. Hernandha, E. Adhitama, J. Kottmeier, A. Dietzel, E. Peiner and H. S. Wasisto, *Commun. Mater.*, 2025, **6**, 32.

24 L. Niu, R. Zhang, Q. Zhang, D. Wang, Y. Bi, G. Wen and L. C. Qin, *Phys. Chem. Chem. Phys.*, 2024, **26**, 17292–17302.

25 J. Zhou, Y. Lan, K. Zhang, G. Xia, J. Du, Y. Zhu and Y. Qian, *Nanoscale*, 2016, **8**, 4903–4907.

26 H. Xue, Y. Cheng, Q. Gu, Z. Wang, Y. Shen, D. Yin, L. Wang and G. Huang, *Nanoscale*, 2021, **13**, 3808–3816.

27 M. H. Saleem, U. Lassi, V. Srivastava and S. Tuomikoski, *J. Power Sources*, 2025, 236879.

28 Z. Zhang, Y. Wu, Z. Mo, X. Lei, X. Xie, X. Xue, H. Qin and H. Jiang, *RSC Adv.*, 2025, **15**, 10731–10753.

29 A. Song, W. Zhang, H. Guo, L. Dong, T. Jin, C. Shen and K. Xie, *Adv. Energy Mater.*, 2023, **13**, 2301464.

30 B. Li, Z. Chen, M. Sun, K. Xie, X. Yang, C. Zhang, X. Cheng, X. Wan, J. Chai, Z. Liu and Y. Zheng, *J. Energy Storage*, 2025, **135**, 118309.

31 Q. Zhan, T. Xu, Z. Zhao, S. Chen, S. Wu and Q.-H. Yang, *Electrochem. Energy Rev.*, 2025, **8**, 27.

32 S. J. Lee, Y. S. Joe, J. S. Yeon, D. H. Min, K. H. Shin, S. H. Baek, P. Xiong, P. Nakhanivej and H. S. Park, *Int. J. Energy Res.*, 2022, **46**, 15627–15638.

33 C. Jin, L. Ma, W. Sun, P. Han, X. Tan, H. Wu, M. Liu, H. Jin, Z. Wu, H. Wei and C. Sun, *Commun. Chem.*, 2019, **2**, 135.

34 J. Zhang, L. Chen, Z.-L. Hou, X. Zhang and C. Li, *J. Energy Storage*, 2024, **87**, 111445.

35 P. Lu, X. Yan, X. Wang, F. Hou and J. Liang, *Sustain. Mater. Technol.*, 2022, **31**, e00375.

36 J. Jiang, J. Liu, W. Zhou, J. Zhu, X. Huang, X. Qi, H. Zhang and T. Yu, *Energy Environ. Sci.*, 2011, **4**, 5000–5007.

37 G. Azuara-Tuexi, E. Muñoz-Sandoval and R. A. Guirado-López, *Phys. Chem. Chem. Phys.*, 2023, **25**, 3718–3736.

38 P. S. Bagus, C. J. Nelin, C. R. Brundle, B. V. Crist, E. S. Ilton, N. Lahiri and K. M. Rosso, *Inorg. Chem.*, 2022, **61**, 18077–18094.

39 A. Aqel, K. M. M. A. El-Nour, R. A. A. Ammar and A. Al-Warthan, *Arab. J. Chem.*, 2012, **5**, 1–23.

40 K. M. Kamal, R. Narayan, S. Periasamy, S. Gyergyek, S. Popović, N. Hodnik, H.-C. Ho, P. Djinović and B. Likozar, *Appl. Catal. O: Open*, 2024, **194**, 206997.

41 M. J. Madito, *Vib. Spectrosc.*, 2025, **139**, 103814.

42 C. Ni, C. Xia, W. Liu, W. Xu, Z. Shan, X. Lei, H. Qin and Z. Tao, *Materials*, 2024, **17**, 754.

43 A. J. Lovett, M. Füredi, L. Bird, S. Said, B. Frost, P. R. Shearing, S. Guldin and T. S. Miller, *ACS Electrochem.*, 2025, **1**, 962–973.

44 Z.-y. Xu, H.-b. Shao and J.-m. Wang, *N. Carbon Mater.*, 2024, **39**, 896–917.

45 J. E. Son, S. G. Im, J.-H. Yim, M. Yang and J.-w. Lee, *Chem. Eng. J. Adv.*, 2024, **20**, 100673.

46 N. Meddings, M. Heinrich, F. Overney, J.-S. Lee, V. Ruiz, E. Napolitano, S. Seitz, G. Hinds, R. Raccichini, M. Gaberšček and J. Park, *J. Power Sources*, 2020, **480**, 228742.

47 J. S. Horner, G. Whang, D. S. Ashby, I. V. Kolesnichenko, T. N. Lambert, B. S. Dunn, A. A. Talin and S. A. Roberts, *ACS Appl. Energy Mater.*, 2021, **4**, 11460–11469.

48 S. Jiang, J. Fan, Y. Liu, T. Zhang, X. Wu, P. Hu, L. Yao, Y. Li, H. Wu, Y. Zhang, Z. Zhou, Y. Zhang and P. Dong, *Adv. Funct. Mater.*, 2026, e19728.

49 Z. Zhang, X. Zhang, Y. Liu, C. Lan, X. Han, S. Pei, L. Luo, P. Su, Z. Zhang, J. Liu, Z. Gong, C. Li, G. Lin, C. Li, W. Huang, M.-S. Wang and S. Chen, *Nat. Commun.*, 2025, **16**, 1013.

50 G. Qian, Y. Li, H. Chen, L. Xie, T. Liu, N. Yang, Y. Song, C. Lin, J. Cheng, N. Nakashima, M. Zhang, Z. Li, W. Zhao, X. Yang, H. Lin, X. Lu, L. Yang, H. Li, K. Amine, L. Chen and F. Pan, *Nat. Commun.*, 2023, **14**, 6048.

51 D. L. Nelson, S. E. Sandoval, J. Pyo, D. Bistri, T. A. Thomas, K. A. Cavallaro, J. A. Lewis, A. S. Iyer, P. Shevchenko, C. V. Di Leo and M. T. McDowell, *ACS Energy Lett.*, 2024, **9**, 6085–6095.

52 J. Zuo, Q. Su, H. Lei, J. Lu, Y.-K. Wang, Z. Ma, X. Cheng, W. Dai, H. Xia, H. Liu, Z. Li and Z. Fu, *Adv. Funct. Mater.*, 2025.

53 L. Chai, X. Wang, C. Bi, B. Su, C. Zhang, X. Li and W. Xue, *ACS Appl. Energy Mater.*, 2023, **6**, 8388–8396.